ACS APPLIED MATERIALS & INTERFACES

Research Article

www.acsami.org

Large-Area Patterning of the Tackiness of a Nanocomposite Adhesive by Sintering of Nanoparticles under IR Radiation

Robert S. Gurney,[†] Damien Dupin,[‡] Elodie Siband,[§] Keltoum Ouzineb,[§,∥] and Joseph L. Keddie*,[†]

[†]Department of Physics, University of Surrey, Guildford, Surrey GU2 7XH, U.K.

[‡]Departamento Nuevos Materiales, IK4-CIDETEC, Parque Tecnológico de San Sebastián, Paseo Miramón, 196, 20009 Donostia, San Sebastián, Spain

[§]Cytec Surface Specialties, Anderlecht Str. 33, Drogenbos B-1620, Belgium

Supporting Information

ABSTRACT: We present a simple technique to switch off the tack adhesion in selected areas of a colloidal nanocomposite adhesive. It is made from a blend of soft colloidal polymer particles and hard copolymer nanoparticles. In regions that are exposed to IR radiation, the nanoparticles sinter together to form a percolating skeleton, which hardens and stiffens the adhesive. The tack adhesion is lost locally. Masks can be made from silicone-coated disks, such as coins. Under the masks, adhesive island regions are defined with the surrounding regions being a nontacky coating. When optimizing the nanocomposite's adhesive properties, the addition of the hard nanoparticles raises the elastic modulus of the adhesive significantly, but adhesion is not lost because the yield point remains relatively low. During probe−tack testing, the soft polymer phases yield and enable fibrillation. After heating under IR radiation, the storage modulus increases by a factor of 5, and the yield point increases nearly by a factor of 6, such that yielding and fibrillation do not occur in the probe−tack testing. Hence, the adhesion is lost. Loading and unloading experiments indicate that a rigid skeleton is created when the nanoparticles sinter together, and it fractures under moderate strains. This patterning method is relatively simple and fast to execute. It is widely applicable to other blends of thermoplastic hard nanoparticles and larger soft particles.

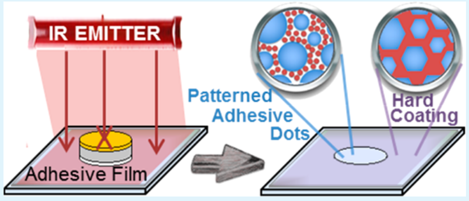

KEYWORDS: *infrared radiation, patterning, tack, nanoparticles, pressure-sensitive adhesives, latex*

Pressure-sensitive adhesives (PSAs) are typically made from viscoelastic polymers that adhere instantly to nearly any surface through van der Waals forces when close contact is made under the application of light pressure. These soft adhesives provide the basis for adhesion in many common products, such as tapes, labels, and graphic displays. They are regularly used to bond together dis-similar objects in lieu of bolts in automotive and aerospace applications.[1] Recently emerging applications of PSAs include transdermal drug delivery[2] and adherent feet for climbing robots.[3,4]

There is a growing need for adhesives that are patterned such that only a portion of their surface is tacky. For instance, electronic components must be attached at specified positions on a breadboard, on which electrically conductive adhesives replace metallic solders.[5−7] PSAs are used to hold components to printed circuit boards prior to soldering, which is highly necessary to avoid misplacement of components during high-speed construction.[8,9] They also provide stress relief to soldered components, preventing premature failure.[10] There are advantages in precisely patterning an adhesive for chip recognition or self-assembly strategies.[11] In biomedical research, there is a need to control precisely the positions of mammalian cell attachment to adhesive surfaces.[12−14] With inspiration from electronics, a "biological breadboard" platform has been developed to regulate cell adhesion through the patterning of adhesive and repulsive regions.[15] In tapes and labels, the modulation of the elastic modulus laterally across a PSA imparts useful peel characteristics.[16]

The patterned adhesion of objects on a substrate can be achieved through the use of adhesive patches or by cutting out portions of a large adhesive sheet to leave adhesive regions at the appropriate locations. In biomedical applications, adhesive molecules have been printed using microcontact methods to create patterns to direct cellular attachment,[17] and adhesive surfaces have been patterned through chemical modifications.[13] Epoxy adhesives for electronics have been patterned with stencils.[18] An alternative approach to patterning adhesives is to create a large-area adhesive surface and then to "switch off" the adhesion in selected regions. In an early example, Geiss and Meyer-Roscher[19] patterned the UV radiation of an adhesive layer to create cross-links only in selected areas, causing a loss of the tack adhesion there. Here, we introduce a new physical method for creating surface coatings with a high tackiness only in selected regions. The mechanism relies on the coalescence of hard nanoparticles heated under infrared radiation. Consequently, it is not restricted to specific polymer chemistries,

Received: December 20, 2012
Accepted: February 21, 2013
Published: February 21, 2013

dx.doi.org/10.1021/am303184k | *ACS Appl. Mater. Interfaces* 2013, 5, 2137−2145

Table 1. Characteristics of the PSA Latex and Hard Nanoparticles

sample description	hydrodynamic diameter[a] [nm]	size polydispersity[a]	solids content [wt %]	gel fraction [wt %]	M_n [g/mol]	M_w [g/mol]	M_w/M_n	T_g[b] [°C]	density [g/cm^3]
poly(butyl acrylate)-rich latex	220	0.09	34 ± 1	18	8300	301 000	36.1	−34.2	1.087
poly(methyl methacrylate)-rich nanoparticle	72	0.08	27 ± 1	0	4570	113 000	24.7	70.6	1.205 ± 0.001[c]

[a] Obtained by dynamic light scattering at 25 °C. [b] Obtained from the dry material using DSC, heating at 10 °C per min. [c] Obtained using helium pycnometry.

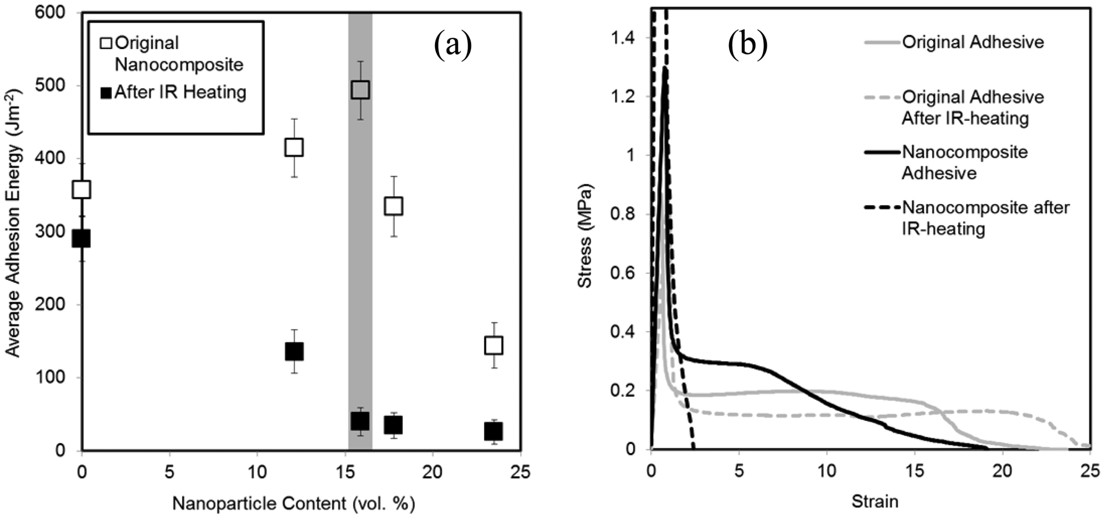

Figure 1. (a) Average adhesion energy for nanocomposite adhesives with varying concentrations of hard nanoparticles before (open square) and after (filled square) IR heating for 30 s. The optimal nanoparticle content (16 vol %) for the greatest differential in tack adhesion is identified in the shaded box. (b) Representative probe−tack debonding curves using a steel probe at 0.1 mm s^{-1} showing tack curves for the optimized nanocomposite (black) and the original adhesive (gray) before (solid) and after IR heating (dashed).

does not require covalent cross-linkers, and is not sensitive to inadvertent UV light exposure.

Our new design concept uses a nanocomposite PSA, which we developed recently,[20] in which hard nanoparticles (having a glass transition temperature, T_g, well above room temperature) are blended with larger particles of a soft polymer, which has a very low T_g. The nanoparticles pack around the larger particles to create a percolating phase. When the nanoparticles are heated above their T_g, they coalesce to form a rigid structure that significantly stiffens the material and thereby switches off the tack adhesion.[20] In this present work, nanocomposite PSAs are heated locally at targeted positions by infrared (IR) radiation shining through masks as a means to pattern the tack adhesion across large areas.

■ RESULTS AND DISCUSSION

Properties of Colloidal Nanocomposite Adhesives. The experiments used a soft poly(butyl acrylate)-rich copolymer latex dispersion having the characteristics listed in Table 1. The viscoelastic properties of this original polymer in the PSA (used previously[20]) are not optimum for achieving high tack adhesion. Nanocomposites were created through the addition of poly(methyl methacrylate)-rich nanoparticles (NPs), with a T_g of 70.6 °C, thus ensuring they are in the glassy state (hard) at room temperature. This T_g was selected with the aim of achieving sintering at lower temperatures and at a faster rate in comparison to our previous work[20] in which the T_g of the NPs was 110 °C. A high size ratio of soft PSA particles to hard NPs of 3:1 was selected to enable efficient packing of the NPs around the PSA particles.

The hard NPs were blended with the adhesive copolymer over concentrations ranging from 12 to 20 vol % as a means to adjust the viscoelasticity (Figure S1, Supporting Information). A similar strategy of adjusting the viscoelastic and adhesive (tack and shear) properties through the inclusion of nanoparticles in a PSA was employed successfully by Bellamine et al.[21] They found that blending in hard nanoparticles increased the shear resistance (i.e., made the adhesive more creep resistant), moderately stiffened the material (increased modulus at low strain), and increased the dissipative properties at large strains by weakening the particle/particle interfaces. Figure S1 (Supporting Information) shows that with the addition of the nanoparticles in our system E' increased, and the ratio of the loss tangent (tan δ) over E', which usually correlates with the tack adhesion energy,[22−24] fell only slightly, as some of the viscous dissipation was lost. Above the optimal nanoparticle concentration, the nanocomposite was far too solid-like for a tacky PSA; E' rose far above the acceptable limit of 0.3 MPa (referred to as the Dahlquist criterion).[25]

The tack adhesion energy was determined for each composition using probe−tack analysis, in which a steel probe was removed from the adhesive surface at a constant velocity, while the force was measured.[26,27] We found that with too few NPs in a nanocomposite the response was too liquid-like: the adhesive created fibrils during debonding, but they were drawn at a low stress value. The probe−tack curves in Figure S2 (Supporting Information) show the effect of the NP addition, and the corresponding variation of the adhesion energy with nanoparticle concentrations is plotted in Figure 1a. In the original PSA, the fibrils can be strained to a relatively high value, but they fail cohesively, leaving residue on the

Table 2. Mechanical and Adhesive Properties of the Original and Nanocomposite Materials: Effect of IR Heating

sample description	Young's modulus (MPa)[a]	storage modulus, E' (MPa)[b]	loss modulus, E'' (MPa)[b]	tan δ[b]	3 tan δ/E' (10^{-6} Pa^{-1})[b]	adhesion energy, E_{adh} (J m^{-2})
original PSA	0.13 ± 0.04	0.23 ± 0.03	0.11 ± 0.03	0.47	6.0	356 ± 36
original PSA − after IR heating	0.11 ± 0.04	0.22 ± 0.03	0.34 ± 0.03	1.58	22.0	290 ± 31
optimized nanocomposite PSA	0.44 ± 0.05	1.31 ± 0.05	0.54 ± 0.05	0.42	1.0	493 ± 40
optimized nanocomposite PSA − after IR heating	2.92 ± 0.05	6.87 ± 0.05	0.97 ± 0.05	0.14	0.06	39 ± 19

[a] Obtained from tensile strain measurements at 1 mm s^{-1} at a temperature of 22 °C. [b] Obtained by DMA at 1 Hz at a temperature of 22 °C.

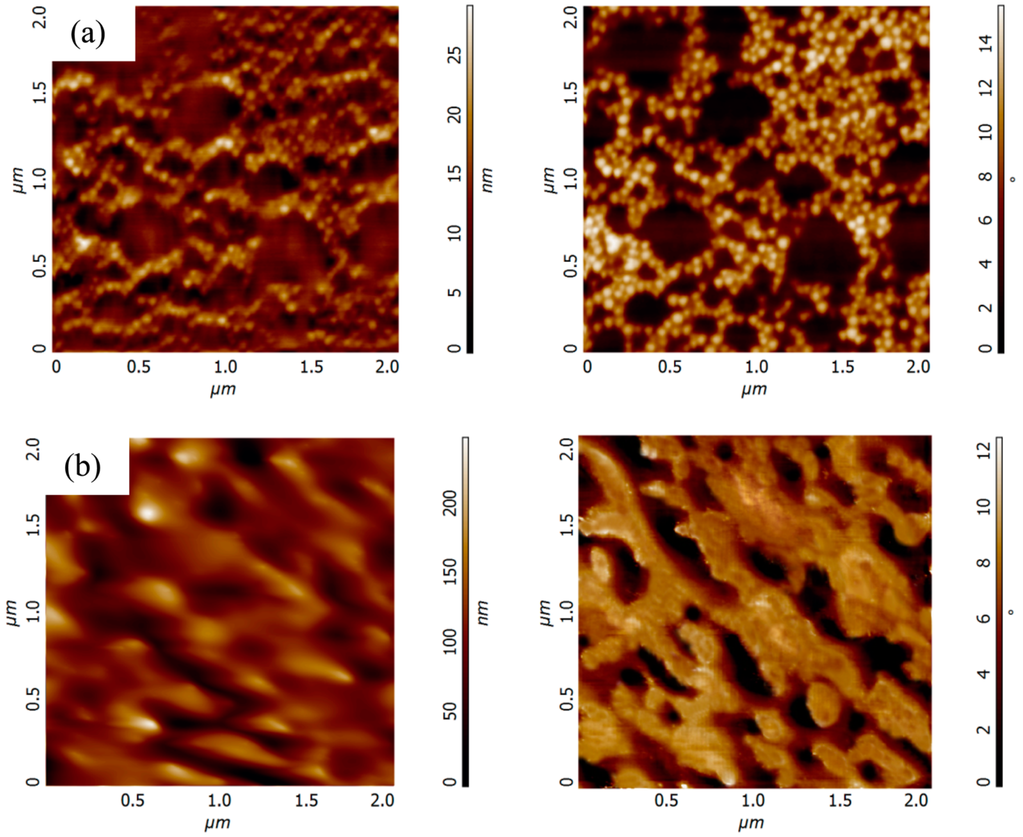

Figure 2. Images (2 μm × 2 μm) of the surface structure of the nanocomposite films, obtained by AFM (a) before and (b) after IR heating for 30 s. Height images are on the left side, and phase images are on the right side. Nanoparticles appear bright in the phase images, and the adhesive particles, which dissipate more energy during scanning, appear dark.

probe. The addition of too many nanoparticles overhardens the nanocomposite, so that although the stress level to draw fibrils during debonding is relatively high the fibrils are not drawn far. Consequently, the adhesion energy is low. The value of the adhesion energy rises from 356 J m^{-2} in the original material to 495 J m^{-2} in the optimum nanocomposite (with 16 vol % NPs), which represents an increase of 40% (Table 2). Representative probe−tack curves for the original PSA and the optimum nanocomposite are compared in Figure 1b. Cohesive failure is similarly observed in the nanocomposite. At lower debonding speeds (1 μm s^{-1}), Bellamine et al.[21] also found a modest increase in the tack adhesion energy when hard nanoparticles were added to a soft matrix, but at higher debonding speeds (1 mm s^{-1}) the effect was lost. In our system, the original PSA is not already optimized for PSA applications; as it is liquid-like, the effects of hard nanoparticles are more noticeable.

The nanocomposite adhesives were heated under IR radiation as a means to switch off the tack adhesion, via the mechanism reported previously.[20] The probe−tack curves in Figure 1b show that at the concentration of 16 vol % NPs there is a complete loss of tack adhesion after IR heating for 30 s. The probe was removed from the surface with no evidence for fibrillation, and the adhesive was not tacky to the touch. The adhesion energy fell from 493 to 39 J m^{-2}, which represents a decrease of 92%, which is the same as previously reported for a similar system.[20] The differential in the tack adhesion before and after IR heating was greatest at the optimum NP concentration of 16 vol % (Figure 1a), and hence it was selected for a subsequent study. (As a control experiment, the original adhesive was also irradiated for 30 s. The stress−strain curve shows that the material softens, and the plateau lengthens, resulting in a 20% drop in the adhesion energy (Figure 1b). This softening of the adhesive phase is fully counter-acted in the nanocomposites by the hardening induced by the nanoparticle sintering.)

Nase et al.[28] showed that the bulk failure of a viscoelastic adhesive (via fibrillation) is favored at low values of $G'd$, where G' is the dynamic shear modulus and d is the film thickness, and at high values of $\mathcal{G}_0$ tan δ, where $\mathcal{G}_0$ is the threshold

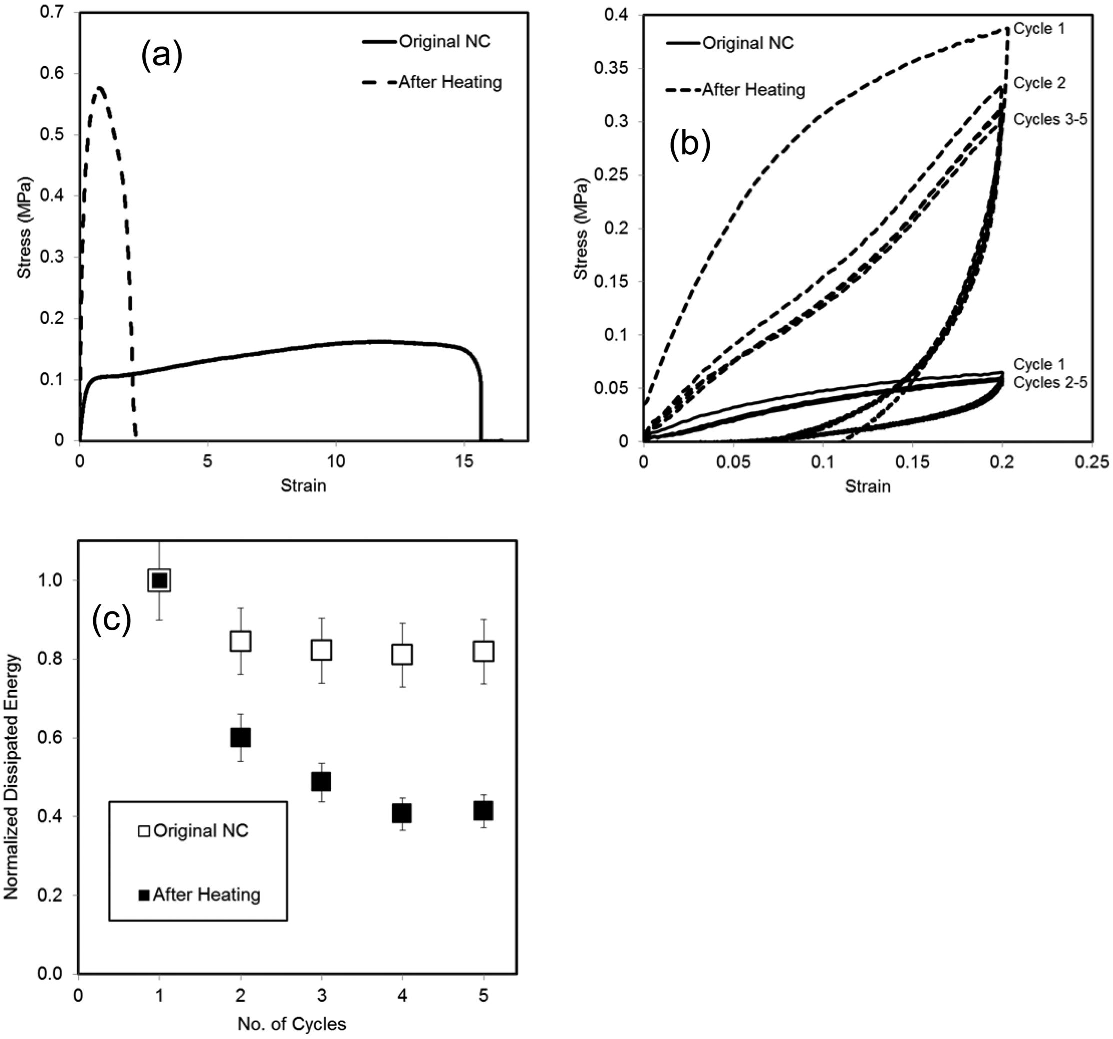

Figure 3. Large-strain deformation for the original nanocomposites (NCs) and those after heating in a convection oven at 140 °C for 30 min. Samples were strained at 1 mm s^{-1} (a) until fracture and (b) to $\varepsilon = 0.2$ before unloading at 0.1 mm s^{-1}. (c) Dissipated energy after each successive loading/unloading cycle, normalized to the first cycle, for the original nanocomposite (NC) and after heating in an oven at 140 °C.

fracture energy, which is a function of the interfacial energies. For a given interface, such that $\mathcal{G}_o$ is constant, and for a given film thickness, bulk failure is therefore favored at higher ratios of $\tan \delta/G'$, whereas interfacial crack propagation is favored at lower ratios. Hence, to switch off adhesion, the ratio should be minimized. Deplace et al.[22] proposed that a fibrillar structure (leading to higher adhesion energy) will develop if $\tan \delta/G' > 0.5 \times 10^{-5}$ Pa^{-1}, when using a steel probe. Letting $G' = E'/3$, Table 2 lists $\tan \delta/(E'/3) = 3 \tan \delta/E'$ as a means of comparing the tendency for fibrillation. This criterion requires the assumption that the materials are purely viscoelastic. (This assumption is reconsidered later in this paper.) For the original PSA, this ratio has a value of 0.5×10^{-5} Pa^{-1}, which situates it in the range where fibrillation will occur, as is observed experimentally. The ratio calculated for the heated nanocomposite is very low (6×10^{-8} Pa^{-1}), which is consistent with the observed interfacial failure and absence of fibrillation. According to this argument, however, it is at first puzzling why fibrillation is observed in the original nanocomposite, despite that $3 \tan \delta/E'$ is measured to be only 0.1×10^{-5} Pa^{-1}, which is below the threshold defined by Deplace et al. This issue will be discussed again later in this article.

IR Heating of Nanocomposite Adhesives to Switch Off Adhesion. Under intense IR radiation for 30 s, the temperature of the adhesive increases at a rate of ca. 10 °C/s before stabilizing at a temperature of 190 °C (Figure S3 in Supporting Information). Although the radiation time is relatively short, an order of magnitude estimate supports the idea that NPs are able to sinter to create a rigid network during this interval. The characteristic time, τ, for particles of radius, R, to sinter, driven by a polymer/air interfacial energy of γ, is given as

$$\tau \sim \eta R/\gamma \tag{1}$$

where η is the viscosity of the material in the particle.[29] The temperature dependence of a polymer's viscosity can be approximated by the WLF equation[30]

$$\eta = \eta_g \exp((-34(T - T_g)/(80 + T - T_g)) \tag{2}$$

where $\eta_g = 6.5 \times 10^{10}$ Pa s. Taking the average temperature under IR radiation, T, to be initially 100 °C and the T_g to be 70 °C for the nanoparticles, η is estimated to be on the order of 6×10^6 Pa s. With $R = 3.5 \times 10^{-8}$ m and taking $\gamma = 3 \times 10^{-2}$ J m^{-2}, we find τ to be on the order of 10 s. Thus, it is realistic for

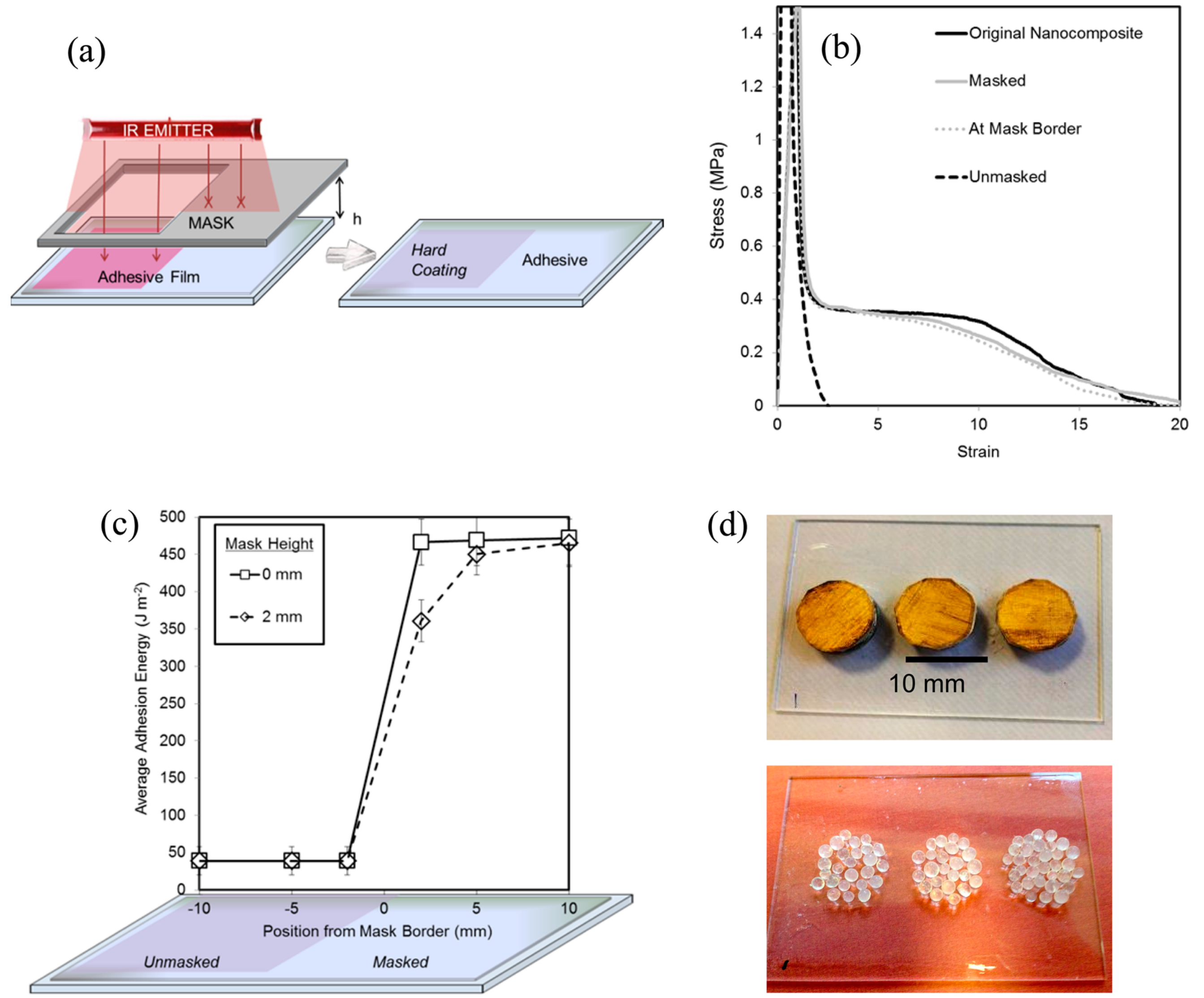

Figure 4. (a) Illustration of the patterning procedure in which a mask is at a height, *h*, above the nanocomposite surface under IR radiation. (b) Representative probe−tack curves showing the original tack adhesion before IR heating (black solid line) and its loss after heating (black dashed line). Curves obtained after IR heating under the masked region (gray) and near the mask border (gray dashed line) are shown for comparison. The mask was resting on the nanocomposite film surface ($h = 0$ mm). (See Figure S3 (Supporting Information) for data at $h = 2$ mm.) (c) The average tack adhesion energies for each position relative to the mask border for the mask at $h = 2$ mm and in contact ($h = 0$ mm). (d) Photographs of a region masked by three gold-coated coins, before and after IR irradiation. Small plastic pellets adhere to the formerly masked regions, but they do not adhere elsewhere on the film surface.

the contacting nanoparticles to sinter together after 30 s of IR radiation.

AFM analysis provides visual evidence for NP sintering. Images in Figure 2a show the NP packing around the large, soft PSA particles in freshly cast films. Individual NPs are clearly resolved and retain their identity; with a T_g of 70 °C, they do not coalesce at room temperature. After heating the film under IR radiation for 30 s (and subsequently cooling to room temperature), NPs can no longer be resolved, indicating that particle sintering has indeed occurred. The hard NP phase extends throughout the softer phase, thus creating a rigid skeleton.

In the initial nanocomposite, the surface coverage of NPs is approximately 46% by area for samples with just 16 vol % NPs. This high surface coverage is indicative of a surface segregation of nanoparticles during the drying phase, which has been attributed by Luo et al. to capillary-driven flow.[31] We calculate that for nanoparticles to create a percolating layer around the larger particles (as was modeled by Kusy[32]) a concentration of approximately 30 vol % is required. This amount rises to 50 vol % to achieve monolayer coverage of all larger PSA particles (see Supporting Information, Figure S4). With only 16 vol % NPs in the blend, it is not possible to have a percolating NP phase throughout the whole depth, but importantly the sintered NPs can nevertheless create a skeletal structure in the upper region of the adhesive.

We note an increase in surface coverage of nanoparticles to 85 area % after IR heating (see Figure 2b), suggesting particle rearrangement during the sintering process, which is presumed to be driven by the surface energy minimization.[33,34] It is known that surfactants and other hydrophilic species are located at the surface of latex particles to ensure colloidal stability, and so the surfaces responsible for the phase restructuring are not only composed of the copolymers.

Tack adhesion is particularly sensitive to the mechanical properties at and near the PSA surface,[21,35,36] along with the bulk material properties,[22,28,37] as it is crucial that the material is soft enough to flow to make close physical contact with the adherent. Because of the enrichment of hard nanoparticles at the nanocomposite surface, a significant change in tack properties is seen at a considerably lower volume fraction of nanoparticles than is predicted by percolation theory.[20,32] Analysis of the nonlinear viscoelasticity of the bulk material was performed to explain the switching mechanism.

In addition to these observed changes in surface nanostructure under IR heating, there were pronounced and important changes in the mechanical properties upon heating bulk materials. These effects are apparent in large-strain tensile tests (Figure 3). The original nanocomposite has a pseudo-yield stress, σ_y, of 0.1 MPa and a Young's modulus (calculated up to a strain of 0.1) of 0.4 MPa. After heating, the nanocomposite exhibits a seven-times higher Young's modulus of 2.9 MPa. The nanocomposite yields at a stress of 0.57 MPa at a strain of approximately 0.5, and it fractures when the strain is increased to higher values, indicating its relative brittleness. In contrast, the original PSA has a lower Young's modulus of 0.13 MPa, which drops slightly to 0.11 MPa after heating.

The strong increase in the yield stress of the nanocomposite after heating offers insight into the switching mechanism. The original nanocomposite has a storage modulus of $E' = 1.31$ MPa, which is far above the limit set by the Dahlquist criterion.[22,25] Yet, acceptable tack adhesion is found, which can be explained by the effect of the combination of hard, mobile nanoparticles in a soft liquid-like matrix. Although the modulus is raised, the yield stress remains low, and fibrillation can occur through yielding of the nanocomposite. In purely elastic materials, cavitation occurs at stress levels above the elastic modulus. However, in viscoelastic-plastic materials, cavitation and fibrillation develop at stresses above σ_y.

Approximating $\mathcal{G}_0$ as 0.1 J m^{-2} for our steel probe (after Nase et al.[28]) and using $h = 10^{-4}$ m, we find that the nanocomposite has the parameters for interfacial failure both before and after heating. However, the equations of Nase et al.[28] and the criteria of Deplace et al.[22] apply for the failure of an elastic material. As the nanocomposites are visco-plastic, as is apparent in their yielding (Figure 3a), we propose to substitute the yield stress, σ_y, for E' in the criteria for fibrillation. We then find for the original nanocomposite that $3 \tan \delta/\sigma_y = 1.3 \times 10^{-5}$ Pa^{-1}, which is in the range where fibrillation is expected to be observed. On the other hand, after heating the nanocomposite, $3 \tan \delta/\sigma_y = 7.6 \times 10^{-7}$ Pa^{-1}, which is consistent with the observation of interfacial crack propagation.[22,28]

In tensile cycling tests (up to strains of 0.2), the nanocomposite, both before and after heating, shows significant hysteresis (Figure 3b); the unloading curves are lower than the loading curves, meaning that there is energy dissipated during the cycle. The nanocomposite does not recover its original dimensions after unloading because of plastic deformation. The postheated nanocomposite exhibits a sharp fall in the elastic modulus after the first deformation but only a slight drop on the second cycle. Thirty-three percent less energy is dissipated when straining the nanocomposite in the second cycle compared to the first cycle (Figure 3c) and around 50% less thereafter. This result can be explained by the existence of a brittle skeletal structure, which is fractured under the tensile strain. In contrast, in the original nanocomposite, there is a weaker decrease in the modulus and in the energy dissipation in the second and subsequent cycles in comparison to the first cycle (Figures 3b and 3c). Although the nanoparticles in the original nanocomposite are percolating, they do not create a rigid structure. There is reversible deformation with some viscoelastic dissipation, but with little permanent damage to the structure, in strains up to 0.2.

Additionally, the linear viscoelasticity that is suitable for an adhesive is transformed by this NP sintering to properties typical of a hard coating. E' for the nanocomposite increases 5-fold to 6.87 MPa (Table 2) after heating, which is far too high for PSA applications. Similar effects on bulk properties were observed at other NP concentrations after heating (Figure S1, Supporting Information).

Large-Area Patterning of Adhesives. We exploited the capability of switching off tack adhesion using IR radiation in the development of a patterning process. We held a metallic IR-opaque mask above the film surface (at a height h, as shown in Figure 4a) to block the radiation in specific regions, thereby preventing heating locally and avoiding the creation of a skeletal nanostructure there. When the mask was placed in direct contact with the adhesive ($h = 0$), there was a negligible change in the probe−tack curves in the masked regions, regardless of the position (Figure 4b). (Silicone-coated paper was fixed to the underside of the mask to prevent it from sticking permanently. If the metallic mask was pressed directly onto the adhesive, there was damage to the surface when lifting it off.) In the unmasked region, a hard coating was formed, and the adhesion energy dropped to 39 J m^{-2}. Figure 4c shows that in regions under a contacting mask at distances of 2, 5, and 10 mm from the edge the adhesion energy is around 470 J m^{-2}, i.e., 95% of the initial value prior to heating. The small drop in adhesion energy can be attributed to the silicone layer perturbing the adhesive surface (and perhaps some transfer of heat by the mask). Note that we are only able to test to a resolution of 2 mm, as this is the approximate contact width of the probe. This experiment provides a proof-of-principle for a method to create patterns of soft adhesive and hard coating regions across a large area.

When the mask was set at $h = 2$ mm, there was evidence for "leakage" of radiated heat into the masked region. Under the mask at a distance of 2 mm from the border, the adhesion energy was reduced to 361 J m^{-2}, which is 73% of the original value. As the distance moving under the mask from the edge increased, the adhesion energy rose. Figure 4c shows that when the mask is in contact with the adhesive the definition of the mask pattern is higher. Simple ray-tracing analysis (Supporting Information, Figure S5) reveals that when the mask is at a height of 2 mm oblique radiation from a 0.7 m long IR emitter extends up to 2 cm underneath the mask edge. The energy density of the IR emitter varies inversely with distance, which results in a lateral temperature gradient underneath the mask. Hence, it can be understood why the adhesive's sintering extends only for distances of a few millimeters under the mask edge. Additionally, the thermal conductivity of the nanocomposite and the substrate will influence the lateral heat flow. Temperature gradients laterally in the plane of the film could potentially lead to gradients in the adhesion energy.

As a demonstration of the utility of the process, small circular metallic disks (with an underlayer of silicone-coated paper) were placed on a nanocomposite surface prior to IR irradiation. The exposed areas hardened to make a tack-free coating. In the areas under the disks, tackiness was retained. Small plastic pellets adhered to the adhesive surface and replicated the pattern created by the disks (Figure 4d).

SUMMARY AND CONCLUSIONS

To summarize, we found that with an optimized particle blend we are able to increase the initial tack adhesion energy by 40% to a value of 493 J m^{-2}. Furthermore, when irradiated under a 4 kW carbon IR emitter for 30 s, the nanoparticles, formerly acting as a filler phase, coalesce and form a rigid structure, which raises the modulus of the PSA, "switching-off" the tack adhesion properties of the film. The tack adhesion energy was reduced to 39 J m^{-2}, i.e., just 8% of the initial value, thereby providing a significantly better switch-off than obtained from a similar nanocomposite in recently published work.[20] Placing an opaque mask in contact with the adhesive during exposure to IR radiation created patterned adhesive regions with a spatial resolution of at least 2 mm.

Patterning of the nanocomposite adhesion is not dependent on a particular polymer chemistry, but rather the new concept relies on a physical mechanism. The method is fast (taking only 30 s), and it is easy to execute, only needing a simple mask (such as coins or a plate with holes) and an IR radiation source. After deposition of a nanocomposite layer, regions can easily be defined to be adhesive, with other regions being nontacky. Our patterned adhesives could be particularly useful in bandages, where they could be individually tailored to fit the contours of a particular wound on a body part, as a means to reduce the pain associated with the bandage removal.[38]

MATERIALS AND METHODS

PSA Latex Preparation. The latex was synthesized using a semicontinuous emulsion polymerization process. Deionized water and seed particles (40 nm) were added to a reactor equipped with a double-jacket heater at 83 °C. Separately, a pre-emulsion of monomer was prepared by adding deionized water, surfactants, a buffer, and the monomers. The mixture of monomers contained *n*-butyl acrylate (*n*-BA), acrylic acid, methyl methacrylate (MMA), and ethyl acrylate, with dodecyl mercaptan (0.05 mol %) to act as a transfer agent to reduce the copolymer chain molecular weight. When the reactor temperature reached 83 °C, an aqueous solution of sodium persulfate and the pre-emulsion were added simultaneously over 4 h. After complete addition of the pre-emulsion and the initiator solution, the reactor was cooled down. The latex dispersion was filtered to remove any coagulum.

Nanoparticle Preparation. The nanoparticles are based on a copolymer of *n*-BA, MMA, and methacrylic acid prepared by emulsion polymerization. Deionized water and the surfactants were added to a 2 L reactor equipped with a double-jacket heated to 80 °C. Separately, in a 2 L cylindrical reactor, a pre-emulsion was prepared by mixing deionized water and surfactants and adding the monomer mixture to the aqueous phase under high shear. When the reactor temperature reached 80 °C, sodium persulfate was added to the initial charge, and the addition of the pre-emulsion was started. After three hours, the dispersion was cooled down and filtered. Characteristics of the nanoparticles are presented in Table 1.

Molecular Weight Distribution Measurement. The number-average molecular weight (M_n), the weight-average molecular weight (M_w), and the polydispersity were determined by conventional gel permeation chromatography (GPC) with polystyrene standards (molecular weight range from 200 to 7.5×10^6 g/mol from EasyCal, Polymer Laboratories). A small portion of the sample was dissolved in tetrahydrofuran and injected into a liquid chromatograph (Merck-Hitachi L7100). The components of the sample were separated by the GPC columns based on their molecular size in solution and analyzed by a refractive index detector. Data were gathered and processed by Cirrus GPC software (Polymer Laboratories).

Particle Size Measurement. The hydrodynamic diameter of the dispersed particles was determined by dynamic light scattering (photon correlation spectroscopy) using a Delsa Nano-C particle sizer (Beckman Coulter). Prior to the measurement, an aliquot of the aqueous dispersion was diluted in the range 0.05 to 1 w/w % using distilled deionized water (Milli-Q, 18 MΩ). The autocorrelation function of the scattered light intensity was recorded at an angle of 165° and used to determine the translational diffusion coefficient and the polydispersity index following a cumulants analysis. The *z*-average particle size was finally returned from the Stokes−Einstein relationship.

Density Measurement. The solid-state densities of the dried nanoparticles were measured at 20 °C using a helium pycnometer (Micrometritics AccuPyc 1330). All measurements were performed three times on 0.12−0.16 g of dry sample.

Gel Content Measurement. Cleaned metallic trays (1.5 cm × 4.5 cm) were coated with the polymer sample and dried at room temperature for 24 h, before being immersed in tetrahydrofuran for 24 h and subsequently dried at 110 °C for 1 h. The nonsoluble fraction was determined gravimetrically from the residual coating mass left on the tray.

Latex/Nanoparticle Blend Preparation. The nanoparticles were blended dropwise with the latex and weighed using a digital laboratory balance. Blends were mixed using a magnetic stirrer bar for 30 min, agitated for a further 2 h, and allowed to rest for 30 min before use.

IR Sintering. Films were heated using a 4 kW carbon mid-IR emitter (Heraeus Noblelight). At its maximum power, the emitter has a temperature of 1200 °C, corresponding to a peak emission wavelength of 2 μm. The emitter has a very fast response time such that it reaches its maximum temperature within 2 s. The lamp was placed 3 cm above the film. At this height, and with an IR emitter power of 4 kW, the IR power density on the film was measured to be 1.7 ± 0.1 W cm^{-2}. Measurements were made using an optical power meter (Anritsu, ML910B) with a sensor for the near-IR range between 0.75 and 1.8 μm (Anritsu, MA9711A).

A 2 mm thick steel plate with a hole in the center (see schematic in Figure 4a) was coated on the underside with a layer of silicone-coated paper. The mask was either placed in direct contact with the film or positioned at a distance of 2 mm above it. Films were heated under the lamp for a period of 30 s before being removed and allowed to cool to room temperature (over a period of 2 h) before use. Masks were also created by sandwiching together two five-pence coins (UK) with silicone-coated paper cut to the same size, placed on the underside. A piece of silicone paper (with a 90 nm gold layer deposited on it by sputtering) was attached to its surface to reflect IR radiation and to minimize the heating of the circular mask.

Probe−Tack Adhesion Analysis. The dispersions were cast on glass substrates using a cube applicator and dried at room temperature for 8 h. All of the dried films had thicknesses, *d*, ranging from 80 to 100 μm, according to measurements with digital calipers, averaged over approximately five measurements. Probe−tack adhesive analysis of the nanocomposite films on glass plates followed the Avery method (Stable MicroSystems Texture Analyzer, Godalming, UK) using a spherical (2.54 cm diameter) steel probe. The probe was lowered onto the film with a load of 4.9 N and allowed 1 s of contact before being withdrawn from the film surface at a constant velocity of 0.1 mm s^{-1} which corresponds to an initial strain rate of approximately 1 s^{-1}. For each sample, four or five replicate measurements were made.

Large-Strain Deformation Testing. Dispersions were cast in poly(tetrafluoroethylene) PTFE molds and dried for seven days at room temperature. Original samples were used as-is, while heated samples were placed in a convection oven at 140 °C for 30 min before removing to fresh air and allowed to cool at room temperature for two hours before use. Strips (15 mm × 3 mm × 1.5 mm measured with digital calipers) were cut from the films. Tests were carried out using a commercial instrument (Stable MicroSystems Texture Analyzer, Godalming, UK). When the ends of the strips were clamped in a tensile geometry, the central portion under strain was 10 mm long. The samples were strained at room temperature at a rate of 1 mm s^{-1} until failure (comparable to the probe−tack debonding rate). Tensile cycling tests were also performed by straining samples past their elastic yield point to an extension of 20% ($\varepsilon = 0.2$) at 1 mm s^{-1} before returning to their original position at a rate of 0.1 mm s^{-1}. This procedure was repeated five times for each sample, with samples being drawn taut between cycles, and their dimensions adjusted accordingly.

Dynamic Mechanical Analysis (DMA). Samples were prepared in the same manner as for large-strain tests. When the ends of the strips were clamped in a tensile geometry, the central portion under strain was 10 mm long. DMA of these strip samples was performed using a commercial instrument (Q800, TA Instruments, New Castle, DE, USA) in isothermal tensile mode at 22 °C with a strain of 0.1% at a frequency of 1 Hz, which is comparable to the strain rate used in the probe−tack measurements.

Atomic Force Microscopy (AFM). To prepare specimens, dispersions were cast on 50 μm thick polypropylene sheets using a spiral bar coater. The same drying process as for films cast on glass substrates was used. Samples were cut to 10 mm × 10 mm and attached to a silicon substrate, which was in turn attached to a metallic base plate. The AFM imaging was conducted in intermittent contact mode on a commercial instrument (NT-MDT Ntegra Prima), using a silicon cantilever with a nominal resonant frequency of 300 Hz (Nanosensors, PPP-NCH-W), force constant of between 10 and 130 N/m, and set point ratio (ratio of free oscillation magnitude to landed magnitude) of 0.75. Height and phase images were recorded and are displayed after third-order 2-D flattening correction using commercial software (Nova, NT-MDT). Nanoparticle surface coverage was calculated by converting images to binary masks using ImageJ (version 1.42) image editing software from the United States National Institutes of Health (http://rsb.info.nih.gov/ij/). The binary mask was created using a Renyi entropy thresholding method to identify the phase image color threshold between hard and soft particles. Error was calculated by standard deviation of the surface coverage for three different areas on each sample.

■ ASSOCIATED CONTENT

Ⓢ Supporting Information

Dynamic mechanical properties for nanocomposites with varying nanoparticle concentrations, before and after heating; representative probe−tack curves for the optimized nanocomposite, before and after heating; temperature profile of a film under IR radiation; estimation of the thickness of surface layers of nanoparticles; representative probe−tack curves of film after irradiation through a mask; calculation of stray IR radiation. This material is available free of charge via the Internet at http://pubs.acs.org.

■ AUTHOR INFORMATION

Corresponding Author

*E-mail: j.keddie@surrey.ac.uk.

Present Address

[||]Toray Films Europe, St Maurice de Beynost, 01708 Miribel Cedex (France).

Author Contributions

The manuscript was written through contributions of all authors. All authors have given approval to the final version of the manuscript.

Notes

The authors declare no competing financial interest.

■ ACKNOWLEDGMENTS

We gratefully acknowledge funding from Cytec Surface Specialties, the Engineering and Physics Sciences Research Council (EPSRC), and METRC for the PhD studentship of R.G. We also acknowledge the EPSRC Knowledge Transfer Account (KTA) at the University of Sheffield for partial funding of D.D.'s industrial secondment. We thank Violeta Doukova and James Skinner (University of Surrey) for experimental assistance, André Utgenannt (University of Surrey) for the IR emitter power density measurement, Andrew Morse (University of Sheffield) for nanoparticle density measurements, and Costantino Creton (ESPCI, Paris Tech) for useful discussions.

■ REFERENCES

(1) Keddie, J. L.; Mallégol, J.; Dupont, O. *Mater. World* **2001**, *9*, 22−24.

(2) Tan, H.; Pfister, W. *Pharm. Sci. Technol. Today* **1999**, *2*, 60−69.

(3) Daltorio, K. A.; Horchler, A. D.; Gorb, S.; Ritzmann, R. E.; Quinn, R. D. *Proc. Int. Conf. Intell. Robots Syst.* **2005**, 3648−3653.

(4) Murphy, M.; W. Tso, W.; Tanzini, M.; Sitti, M. *Proc. Int. Conf. Intell. Robots Syst.* **2006**, 3411−3416.

(5) Gallagher, C.; Matijasevic, G.; Maguire, J. F. *Proc. Elec. Compon. Technol.*, San Jose, CA, 1997; pp 554−560.

(6) Whalley, D. C.; Mannan, S. H.; Williams, D. J. *Assem. Automot.* **1999**, *17*, 66−74.

(7) Ogunjimi, A. O.; Mannan, S. H.; Whalley, D. C.; Williams, D. J. *IEEE Trans. Comp. Packag. Manuf. Technol. C* **1996**, *19*, 257−263.

(8) Derebail, A.; Srihari, K.; Emerson, C. R. *Int. J. Adv. Manuf. Technol.* **1994**, *9*, 93−105.

(9) Marongelli, S. R.; Dixon, D.; Porcari, S.; Cummings, W.; Murch, F.; Osterhout, A. *Proc. IEEE/CPMT Int. Electron. Manuf. Technol. Symp.* **1998**, 147−155.

(10) Gould, J. *Polym. Electron.* **2004**, 1−6.

(11) Northen, M. T.; Turner, K. L. *Nanotechnology* **2005**, *16*, 1159−1166.

(12) Luebke, K. J.; Carter, D. E.; Garner, H. R.; Brown, K. C. *J. Biomed. Mater. Res., Part A* **2004**, *68*, 696−703.

(13) Ku, S. H.; Lee, J. S.; Park, C. B. *Langmuir* **2010**, *26*, 15104−15108.

(14) Ruardij, T. G.; Goedbloed, M. H.; Rutten, W. L. C. *IEEE Trans. Biomed. Eng.* **2000**, *47*, 1593−1599.

(15) Yoon, S.-H.; Chang, J.; Lin, L.; Mofrad, M. R. K. *Lab Chip* **2011**, *11*, 3555−3562.

(16) Ghatak, A. *Phys. Rev. E* **2010**, *81*, 1−6.

(17) Chien, H.-W.; Kuo, W.-H.; Wang, M.-J.; Tsai, S.-W.; Tsai, W.-B. *Langmuir* **2012**, *28*, 5775−5782.

(18) Miric, A. Z. *Solder Surf. Mount Technol.* **1996**, *8*, 49−51.

(19) Geiss, P. L.; Brockman, W.; Meyer-Roscher, B. D. *Hot Melt Symp.*; Tappi Press: Georgia, 1998; pp 43−52.

(20) Gurney, R. S.; Dupin, D.; Nunes, J. S.; Ouzineb, K.; Siband, E.; Asua, J. M.; Armes, S. P.; Keddie, J. L. *ACS Appl. Mater. Interfaces* **2012**, *4*, 5442−5452.

(21) Bellamine, A.; Degrandi, E.; Gerst, M.; Stark, R.; Beyers, C.; Creton, C. *Macromol. Mater. Eng* **2011**, *296*, 31−41.

(22) Deplace, F.; Carelli, C.; Mariot, S.; Retsos, H.; Chateauminois, A.; K. Ouzineb, K.; Creton, C. *J. Adhes.* **2009**, *85*, 18−54.

(23) Wang, T.; Lei, C.-H.; Liu, D.; Manea, M.; Asua, J. M.; Creton, C.; Dalton, A. B.; Keddie, J. L. *Adv. Mater.* **2008**, *20*, 90−94.

(24) Wang, T.; Colver, P. J.; Bon, S. A. F.; Keddie, J. L. *Soft Matter* **2009**, *5*, 3842.

(25) Dahlquist, C. A. In *Treatise on Adhesion and Adhesives*; Patrick, R. L., Ed.; Dekker: New York, 1969; Vol. 2, pp 219−260.

(26) Lakrout, H.; Sergot, P.; Creton, C. *J. Adhes.* **1999**, *69*, 307−359.

(27) Zosel, A. *Int. J. Adhes. Adhes.* **1998**, *18*, 265−271.

(28) Nase, J.; Lindner, A.; Creton, C. *Phys. Rev. Lett.* **2008**, *101*, 074503.

(29) Routh, A. F.; Russel, W. B. *Langmuir* **1999**, *15*, 7762−7773.

(30) Larson, R. G. *The Structure and Rheology of Complex Fluids*; Oxford University Press: New York, 1998; pp 130−132.

(31) Luo, H.; Cardinal, C. M.; Scriven, L. E.; Francis, L. F. *Langmuir* **2008**, *24*, 5552−61.

(32) Kusy, R. P. *J. Appl. Phys.* **1977**, *48*, 5301−5305.

(33) Jones, R. A. L.; Richards, R. W. *Polymers at Surfaces and Interfaces*; Cambridge University Press: UK, 1999; pp 36−44.
(34) Wu, S. *Polymer Interface and Adhesion*; Marcel Dekker: New York, 1982; pp 169−211.
(35) Diethert, A.; Ecker, K.; Peykova, Y.; Willenbacher, N.; Müller-Buschbaum, P. *ACS Appl. Mater. Interfaces* **2011**, *3*, 2012−2021.
(36) Carelli, C.; Déplace, F.; Boissonnet, L.; Creton, C. *J. Adhes.* **2007**, *83*, 491−505.
(37) Chang, E. *J. Adhes.* **1997**, *60*, 37−41.
(38) Klode, J.; Schöttler, L.; Stoffels, I.; Körber, A.; Schadendorf, D.; Dissemond, J. *J. Eur. Acad. Dermatol. Venereol.* **2011**, *25*, 933−939.